Article

Numerical Investigation on the Influence of Breakwater and the Sediment Transport in Shantou Offshore Area

Yuxi Wu [1], Kui Zhu [2,*], Hao Qin [1], Yang Wang [3], Zhaolong Sun [2], Runxiang Jiang [2], Wanhu Wang [3], Jiaji Yi [3], Hongbing Wang [3] and Enjin Zhao [1]

[1] College of Marine Science and Technology, China University of Geosciences, Wuhan 430074, China
[2] College of Electrical Engineering, Naval University of Engineering, Wuhan 430033, China
[3] Haikou Marine Geological Survey Center, China Geological Survey, Haikou 570100, China
* Correspondence: zeek@cug.edu.cn

Abstract: The coastline of Shantou is tortuous, while the hydrodynamic environment is complicated. In this paper, the hydrodynamic model is established by the FVCOM (Finite Volume Coastal Ocean Model); the open boundary conditions such as water level, river, and wind field are the input; and the model is verified by tidal harmonic function. According to the previous research, the typhoon wind field with a 10-year return period is selected for storm surge simulation. When there is a bank, the accumulated water on the land cannot enter the ocean due to the block of the bank but accumulates on the inner side of the bank, resulting in higher accumulated water, but less than 0.5 m. In the aspect of sediment deposition, a sediment transport model is established to analyze the sediment deposition in Shantou Port and its surrounding waters. Some reasonable suggestions are put forward for the sediment deposition in Shantou. According to the simulation results, the following conclusions can be drawn: (1) In the case of typhoon storm surge in the return period of 10 years, the bank can effectively protect the inland. Still, accumulated water will collect near the bank. (2) The offshore water level will rise by 0.4 m after adding a bank. (3) The sediment in Shantou Bay mainly comes from the ocean sediment caused by tides, and the largest sedimentation occurs in the main channel.

Keywords: numerical simulation; hydrodynamic force; sediment transport; embankment

1. Introduction

The coastline of China is twisty and turning, and foreign trade in coastal areas prospers. The economy develops rapidly but is also threatened by marine disasters [1], among which the storm surge brings the most severe losses [2–4]. The post-disaster reconstruction after the storm surge requires a large number of materials and personnel investment. Storm surges are generally caused by typhoons [5]. In summer, the southeast coast of China is easily attacked by tropical cyclones, causing massive casualties. As a typical coastal special economic zone in China, Shantou has experienced many typhoons landing [6]. The accompanying storm surges cause heavy financial losses and often cause thousands or even tens of thousands of casualties.

The formation and development mechanism of storm surge was put forward in the early 20th century. Firstly, the theoretical storm surge model was put forward, which was constantly supplemented and improved, and its mechanism was deeply discussed [7]. With the rapid development of geodetic techniques, the research on numerical models has been deepened. Since the 21st century, many numerical models for storm surge models have existed. For example, the POM (Princeton Ocean Model) and the improved ECOM (Estuary Coast and Ocean Model) of Princeton University in the United States are three-dimensional baroclinic models; the Delft-3D model of Delft Water Conservancy Research Institute in the Netherlands; HAMSOM (Hamburg Shelf Ocean Model) developed by the University of Hamburg, Germany; and the FVCOM (An Unstructured Grid Finite Volume Coastal Ocean

Model) of the Massachusetts Institute of Technology are all models used previously [8–10]. The storm surge model in this paper is based on the FVCOM model and is coupled with the typhoon data of a 10-year return period has been verified in the reference.

In order to resist the storm surge, many scholars put forward coastal port facilities protection measures and disaster reduction measures [11–13]. Currently, there are mainly two kinds of protection against storm surges: one is to set up a bank, and the other is to build an ecological vegetation coast [14]. The former is a traditional protective measure that can weaken the waves caused by the storm surge. It has a positive effect in weakening the storm surge, but its influence range is limited, and it has little impact on the sea area far away from the shoreline [15–17]; the latter is that blueprint of green seawall recently put forward, and the previous study have shown that salt marsh vegetation can attenuate tidal current velocity, and a model that can be used to study the interaction mechanism between wetland vegetation and hydrodynamic forces during storm surge transit has been established [18]. In this paper, we consider the effectiveness of setting up the embankment to weaken the storm surge under the typhoon storm surge model with a 10-year return period.

No matter whether the embankment is set up or the vegetation is covered, it belongs to human activities, which will destroy the original coastline in this area, leading to the reduction of the sea area and the tidal volume in the bay, thus affecting the sediment carrying capacity of the sea area, accelerating the sediment deposition rate in the bay [19], and changing the coastline shape again, forming the positive feedback of sediment deposition. Therefore, coastal cities are affected by human activities in bays, estuaries, and ports, and sediment deposition often occurs. It is necessary to analyze and evaluate the sediment in the port area to protect the topography and ecological environment of the basin. Tides usually control the deposition, so the sediment model needs to be coupled with the hydrodynamic model for overall analysis [20–23]. Currently, the widely used sediment transport models include the MIKE model, MOHID model, ECOM, FVCOM, Delft3D model, etc. [24–26]. The sediment models at the port are complicated and are affected by three factors: topography, hydrodynamics, and sediment conditions. Aiming at the problem of sediment deposition in Shantou Port, many scholars have conducted detailed and precise research on sediment deposition in Shantou Port [27,28]. Still, the research time is relatively old, and due to the interference of human activities, the water area of Shantou Port is constantly shrinking, and the hydrodynamic conditions are continually changing. Therefore, it is necessary to build a new model of sediment deposition in Shantou Port in time.

In this paper, the hydrodynamic model of Shantou offshore is established, and the model is verified by the tidal harmonic constant. Based on the hydrodynamic model, according to the study of the Shantou storm surge model by Tang Yue Zhao, a 10-year return period typhoon storm surge model is established. The situation of storm surge increasing water and causing disasters in the 10-year return period is analyzed in the circumstance of deposition. At the same time, the sediment transport model is established and verified. The sediment deposition in Shantou Bay and surrounding waters are analyzed using the model, and the causes of sediment deposition are analyzed.

2. Model Introduction and Verification

2.1. Hydrodynamic Model

This paper uses FVCOM to simulate the ocean hydrodynamic forces, which is a prediction model for the ocean hydrodynamic environment in offshore areas and estuaries [29]. FVCOM adopts the finite volume method, uses unstructured triangular mesh to solve the original equation discretely, and encrypts the research area locally. On the one hand, the finite volume method can discretely solve the variables of the original equation. On the other hand, it can ensure efficient calculation when the equation is integrated, which fully uses the respective advantages of the finite element method and the finite difference method [30]. In the Cartesian coordinate system, the governing equations of FVCOM

include the continuity equation, momentum conservation equation in three directions, temperature and salinity conservation equation, and density equation.

$$\frac{\partial u}{\partial x} + \frac{\partial v}{\partial y} + \frac{\partial w}{\partial z} = 0 \tag{1}$$

$$\frac{\partial u}{\partial t} + u\frac{\partial u}{\partial x} + v\frac{\partial u}{\partial y} + w\frac{\partial u}{\partial y} - fv = -\frac{1}{\rho_0}\frac{\partial P}{\partial x} + \frac{\partial}{\partial z}(K_m\frac{\partial u}{\partial z}) + F_u \tag{2}$$

$$\frac{\partial v}{\partial t} + u\frac{\partial v}{\partial x} + v\frac{\partial v}{\partial y} + w\frac{\partial v}{\partial z} + fu = -\frac{1}{\rho_0}\frac{\partial P}{\partial y} + \frac{\partial}{\partial z}(K_m\frac{\partial u}{\partial z}) + F_v \tag{3}$$

$$\frac{\partial P}{\partial z} = -\rho g \tag{4}$$

$$\frac{\partial T}{\partial t} + u\frac{\partial T}{\partial x} + v\frac{\partial T}{\partial y} + w\frac{\partial T}{\partial z} = \frac{\partial}{\partial z}(K_h\frac{\partial T}{\partial z}) + F_T \tag{5}$$

$$\frac{\partial S}{\partial t} + u\frac{\partial S}{\partial x} + v\frac{\partial S}{\partial y} + w\frac{\partial S}{\partial z} = \frac{\partial}{\partial z}(K_h\frac{\partial S}{\partial z}) + F_S \tag{6}$$

$$\rho = \rho(T, S) \tag{7}$$

Equation (1) is a continuity equation, where x, y, and z represent the positions in the east-west direction, north-south direction, and vertical direction in the Cartesian coordinate system. u, v, and w represent the velocity components in three directions in the Cartesian coordinate system. Equations (2)–(4) are momentum conservation in the east-west direction, north-south direction, and vertical direction, respectively, and F represents the parameter of geostrophic deflection force; ρ is the density of local seawater and ρ_0 is the density of reference position; P is pressure; K_m is the vertical eddy viscosity coefficient; G is the acceleration of gravity; F_u, F_v, F_T, and F_S are diffusion terms of momentum, temperature, and salinity in two horizontal directions, respectively. Equations (5)–(7) are the temperature equation, salinity equation, and density equation, respectively. T is temperature, S is salinity, and K_h is the vertical diffusion coefficient of turbulent kinetic energy.

In the actual simulation process, the natural seabed terrain is often uneven. In order to avoid the false flow and diffusion caused by the rough bottom of the model, it is necessary to transform the σ coordinate vertically to smooth the bottom.

$$\sigma = \frac{z - \zeta}{H + \zeta} = \frac{z - \zeta}{D} \tag{8}$$

Equation (8) is the conversion between the σ coordinate and Cartesian coordinate, where z is the specific position of the Cartesian coordinate system or the height of the water surface relative to the still water, H is the distance from the reference surface to the seabed, and D is the height of the total water column. Under the condition of this coordinate system, the variation range of σ is from 0, indicated by seawater, to -1 at the bottom of the ocean, which avoids the unevenness of the bottom in the original Cartesian coordinate system.

2.2. Typhoon Model

According to the previous research, this paper uses the Holland typhoon model to construct the typhoon wind field with a frequency of 10 years. The model typhoon center pressure is 947 hPa, and the maximum wind speed is 47.26 m/s. The governing equation of the model is as follows:

$$P_r = P_c + (P_n - P_c)\exp(-(R_{\max}/r)^B) \tag{9}$$

$$V_r = [\frac{B}{\rho_a}(\frac{R_{\max}}{r})^B(P_n - P_c)\exp[-(\frac{R_{\max}}{r})^B] + (\frac{rf}{2})^2]^{0.5} - \frac{rf}{2} \tag{10}$$

Equation (9) is the pressure distribution formula of the Holland typhoon model, where P_c is the lowest pressure in the typhoon center and P_n is the background pressure, at 1013 hPa; $R_{\max}$ is the maximum wind speed radius of the typhoon; r is the distance from somewhere to the typhoon center; B is the scale parameter of the typhoon model. Equation (10) is the wind speed distribution formula of the typhoon model, where the air density (ρ_a) is 1.2 kg/m³; f is the parameter of Coriolis force.

There are many formulas to determine the maximum wind speed radius of the typhoon, such as Graham, Tang Jian, Jiang Zhihui, etc. [31–33], and all put forward corresponding formulas. In this study, the procedure proposed by Willoughby [34] is adopted to determine the maximum wind speed radius of a typhoon:

$$R_{\max} = 51.6 \exp(-0.0223 V_{\max} + 0.0281\varphi) \tag{11}$$

where φ is the latitude of the place where the typhoon center is located.

The maximum wind speed ($V_{\max}$) of the typhoon is constructed according to the relationship between wind speed and air pressure proposed by Atkinson-Hollidy [35], and the empirical formula is given:

$$V_{\max} = 3.7237 \times (P_n - P_c)^{0.6065} \tag{12}$$

2.3. Sediment Model

This paper uses MIKE software's ST (sediment transport) module to calculate sediment transport. The open boundary of the sediment model is driven by the calculation result of the FVCOM hydrodynamic model, and the wind field data are reanalyzed by ECMWF. MIKE FVCOM and Mike FVCOM use unstructured grids and finite volume methods to solve discrete integrals so they can share the same grid system. The governing equation of the sediment model is as follows:

$$\frac{\partial \overline{c}}{\partial t} + u\frac{\partial \overline{c}}{\partial x} + v\frac{\partial \overline{c}}{\partial y} = \frac{1}{h}\frac{\partial}{\partial x}\left(hD_x\frac{\partial \overline{c}}{\partial x}\right) + \frac{1}{h}\frac{\partial}{\partial y}\left(hD_y\frac{\partial \overline{c}}{\partial y}\right) + \frac{F_S}{h} \tag{13}$$

Equation (13) is the sediment transport formula of the model, where the average sediment concentration is; u and v are the average vertical velocities in the x and y directions, respectively; h is the water depth there; D_x and D_y are turbulent diffusion coefficients of sediment in two directions, respectively; F_S is a function term of sediment source.

Sediment source function F_S is defined by the following formula:

$$F_s = \begin{cases} E(\tau_b/\tau_{ce} - 1)^n & \tau_b > \tau_{ce} \\ 0 & \tau_{ce} \geq \tau_b \geq \tau_{cd} \\ \omega_s c_b p_d & \tau_b < \tau_{cd} \end{cases} \tag{14}$$

where E the sediment scouring coefficient of the bottom of the river is bed; ω_s is the settling velocity of sediment, which is related to the shape, size, and content of sediment particles. p_d is the possible settlement probability; τ_b is the shear stress at the bottom of the bed; τ_{ce} is the critical shear stress initiated by surface sediment; τ_{cd} is the acute shear stress at which suspended sediment begins to settle.

The range of the sediment transport model (Figure 1) selects Shantou Port, including the Rongjiang River and Hanjiang River and its surrounding waters. Based on the hydrodynamic model, rivers are added. The study area is narrowed. Thus, the running time of the model is shortened, and the accuracy of the key research area is improved.
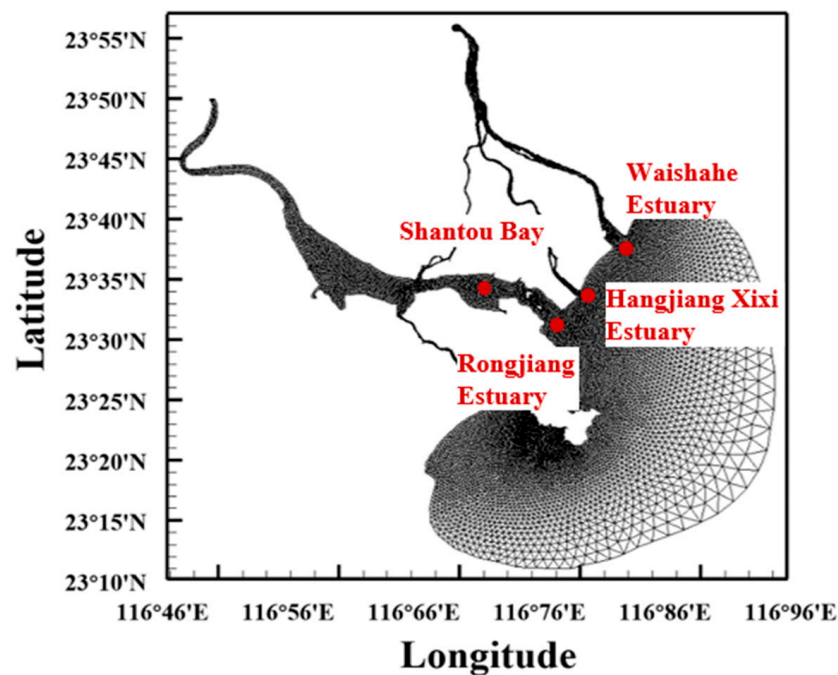
Figure 1. Grid of sediment transport model.

3. Verification of the Model

3.1. Verification of Tidal Harmonic Constant

The tidal harmonic constant of the interpolated hydrodynamic model is verified to prove the validity of the model. In this paper, three long-term tidal stations in the study area are selected, namely Yunaowan Tidal Station (117°06′ E, 23°24′ N), Shantou Tidal Station (116°44′ E, 23°20′ N), and Haimen Tidal Station (116°37′ E, 23°11′ N). In the model of the previous section, the tidal level data of three tide points are derived. The measured tidal level data and the derived tidal level data are calculated by the T-tide program, and the tidal harmonic constants of the corresponding positions are obtained. The simulation results are compared with the measured results' tidal harmonic constants of the four main tidal components K1, O1, M2, and S2. See Table 1 for the verification results of the model. It can be seen from the table that the amplitude error of other tidal components is less than 4 cm, and the late angle error is less than 12 degrees, except for M2, which is slightly larger. The mistake of the Shantou tide gauge station is somewhat more prominent, influenced by its geographical location. Generally speaking, the tidal harmonic constant error between the simulated and the measured results is within an acceptable range, which means that the model has sure accuracy and credibility.

3.2. Verification of Deposition Rate

The sediment transport model is verified by calculating the change of sediment thickness in Shantou Port in the simulation results (Figure 2). The simulation is from 1 January 2015 to 31 December 2019. Shantou Port's natural sediment deposition and surrounding waters are simulated without human intervention. Through calculation, the average deposition thickness of Shantou Port in five years is 0.416 m, and the average annual deposition thickness is 8.3 cm. The siltation speed of Shantou Port has been impacted by human activity throughout history, as evidenced by available data [27]. It can be roughly estimated that, if the initial conditions, such as water area and sediment content of Shantou Port, are constant, the average deposition thickness from 2015 to 2019 should be about 9 cm, slightly higher than the model simulation results. We are assuming that the initial conditions, such as water area and sediment content of Shantou Port, are constant at the beginning of the People's Republic of China. The average deposition thickness from 2015 to 2019 should be about 9 cm, slightly higher than the model simulation results. However, considering the

breakwater construction, part of the sediment entering the port will settle at the estuary, resulting in the real sedimentation rate being lower than the estimated value. Therefore, the research model is more accurate.

**Table 1.** Verification of tidal harmonic constant.

Constituent	Tide Station	Measured Amplitude (°)	Simulated Amplitude (°)	Error (m)	Measured Epoch (°)	Simulated Epoch (°)	Error (m)
K1	Yunaowan	36.04	36.93	0.89	287.02	286.31	0.71
	Shantou	32.13	22.89	9.24	301.74	293.57	8.17
	Haimen	33.42	32.35	1.07	290.62	288.48	2.14
O1	Yunaowan	25.43	25.53	0.10	241.82	241.10	0.72
	Shantou	22.16	15.62	6.54	254.45	250.87	3.58
	Haimen	22.72	22.03	0.69	242.10	242.80	0.70
M2	Yunaowan	57.94	68.79	10.85	7.27	10.70	3.43
	Shantou	32.89	49.40	16.51	26.38	20.30	6.08
	Haimen	26.51	35.57	9.06	11.35	15.26	3.91
S2	Yunaowan	10.79	14.79	4.00	73.42	73.78	0.36
	Shantou	7.66	8.52	0.86	100.68	87.19	13.49
	Haimen	4.13	9.16	5.03	95.86	86.66	9.20
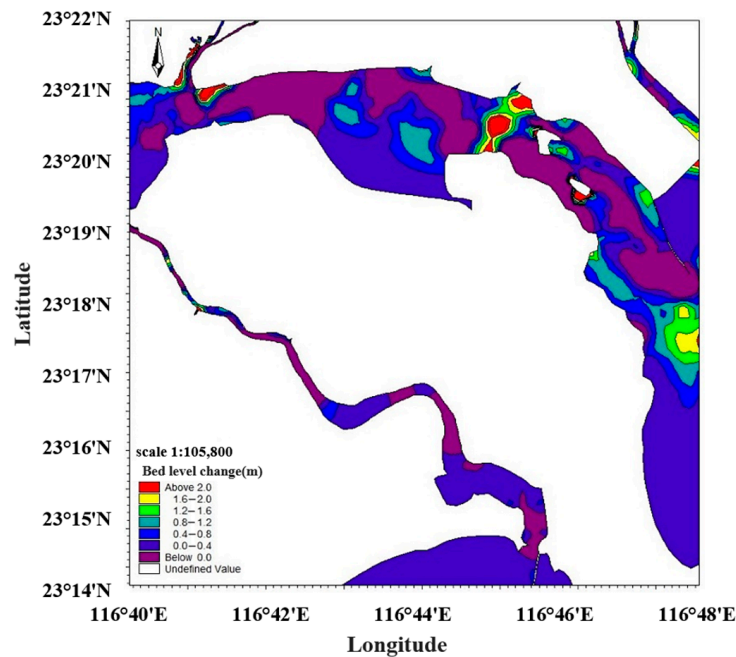
**Figure 2.** Changes of the bed bottom in the Shantou Port in five years.

4. Model Area and Data

The study area is from 116°22′ E west to 117°48′ E in the east and from 22°68′ N in the south to 23°73′ N in the north, including Shantou's offshore and surrounding waters. We used SMS (surface-water modeling system) software to lay unstructured triangular grids. The density of open boundary nodes decreases gradually from land to sea, which can improve computational efficiency while encrypting the critical research areas. The grid resolution in the coastal part of the open boundary is high, and the grid resolution in the main study area near the coastal area of Shantou City is up to 100 m. The research area grid contains 55,790 computing nodes and 108,354 irregular triangular grids (Figure 3). Considering that the research object belongs to the ocean surface, it is divided into five σ layers vertically.
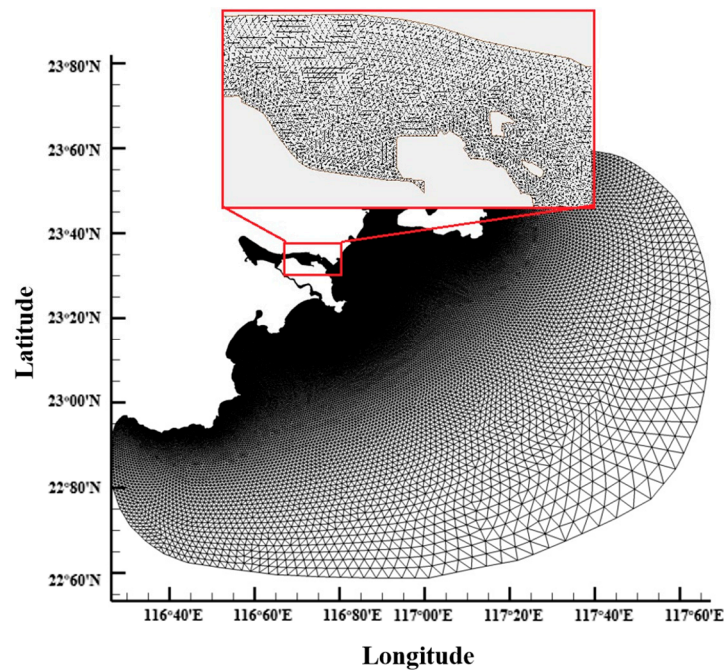
Figure 3. Grid setting in Shantou offshore (the red box in the figure is the coastal area of Shantou City where the grid resolution is up to 100 m).

High-precision data are an essential condition for the model to obtain reliable results. The water depth data in this paper adopt the global seabed topographic data of ETOPO1 provided by the NOAA (National Ocean and Atmospheric Administration) and the chart-sounding data with the number 81001. The ETOPO1 data have the highest accuracy among ETOPO data, with a spatial resolution of $1/60° × 1/60°$. The bathymetric data of the chart are the measured data, which have a high density in the coastal areas. The datum plane of ETOPO1 data is the global mean sea level, while the datum plane of the chart is the local mean tide height datum plane. After conversion, the tide level starting surface of Shantou City is uniformly used as the datum plane, Figure 4 shows the water level in Shantou offshore and Figure 5 shows the study area after inserting topographic data.
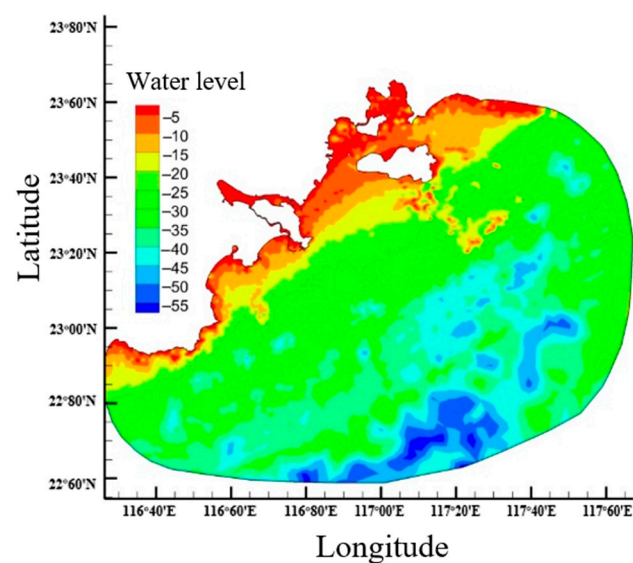
Figure 4. Bathymetric chart (The figure shows the water level in Shantou offshore. The colder color means a deeper water level).
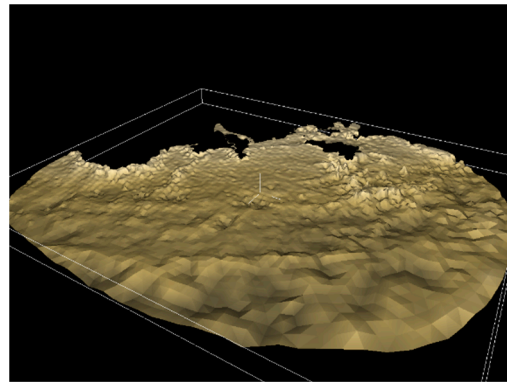
Figure 5. Terrain of the study area.

5. Results of Typhoon Storm Surge Simulation

5.1. Analysis of Typhoon Storm Surge Disasters with Different Intensities

According to the statistics of tropical cyclones in Shantou since the founding of the People's Republic of China, Tang Yue Zhao designed storm surge models in Shantou with different return periods combined with the Holland typhoon model and simulated storm surge with parametric typhoon models. It was found that southeast-west typhoons were the most common, and the typhoon center pressures corresponding to the return periods of 10 years, 50 years, 100 years, and 1000 years were 947 hPa, 937 hPa, 920 hPa, and 905 hPa, respectively [36]. The maximum water increase in different return periods is obtained from the four stations of Nan'ao Station, Chaoyang District, Chenghai District, and Shantou Port as shown in Figure 6.
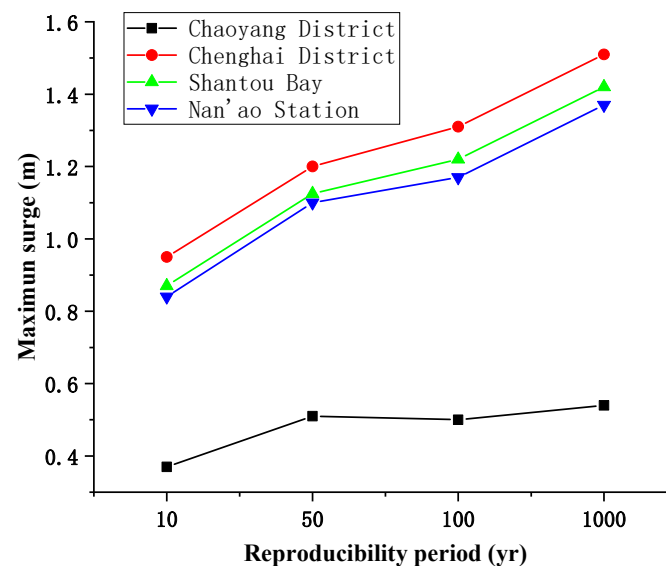

Figure 6. The maximum water increase in different return periods is obtained from the four sta-tions of Nan'ao Station, Chaoyang District, Chenghai District, and Shantou Bay (The maximum water increase is shows an increasing trend with the increase of return period years).

In actual working conditions, the probability of a storm surge of more than 100 years is low, and the port project cannot cope with the storm surge of a 100-year return period [37,38]. According to the research results of Tang Yue, this paper selects the typhoon moving from southeast to northwest in the 10-year return period and analyzes the protection effect of setting the bank dike on Shantou. To make the simulation results of typhoons and storms more intuitive, the north latitude range is 23°33′ N to 23°45′ N and the west longitude from 116°66′ E to 116°84′ E is selected for local simulation. Some grids in the main urban

area of Shantou extend inland based on the original coastline. At the same time, Shantou's coast is artificial, so the actual shoreline is changed to a bank embankment with a height of 1.5 m. When the external water level is less than 1.5 m, it is regarded as a solid boundary where no water exchange occurs. The standard simulation calculation is carried out when it is higher than 1.5 m. The extended part is shown in Figure 7. The grid extending to the land is in the red line in the figure. The land elevation data are obtained by combining the extracted remote sensing data with the measured elevation data. The red line in the figure is the original shoreline, the dam is set in the model, and its height is set to be 1.5 m higher than the average sea level.
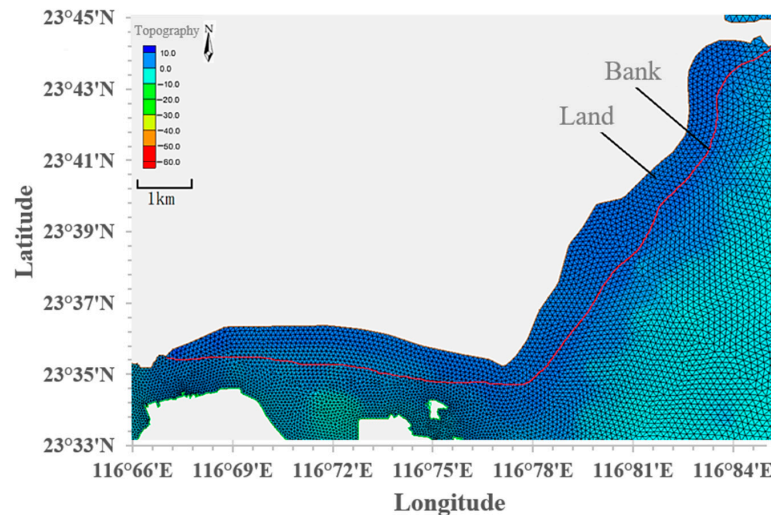

Figure 7. Urban coastal grid expansion (The red line in the figure is the original shoreline, the dam is set in the model, and its height is set to be 1.5 m higher than the average sea level).

Figure 8 shows the distribution of water level and flow field in the Shantou sea area and the inundation of storm surge on the coast and land under the southeast-northwest route during the 10-year return period of typhoon storm surge. The center of the typhoon landed in Chenghai District, Shantou City. Under this path, the hurricane hit Shantou City head-on, which has an excellent representative significance. The simulation time is 72 h, of which 48 to 72 h is the transit time of typhoons.
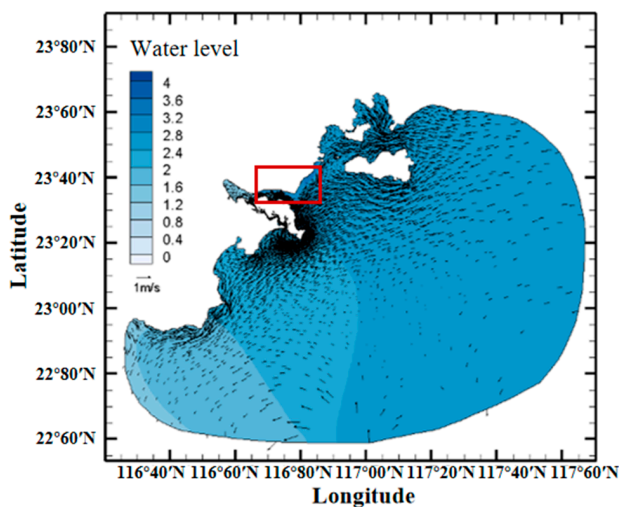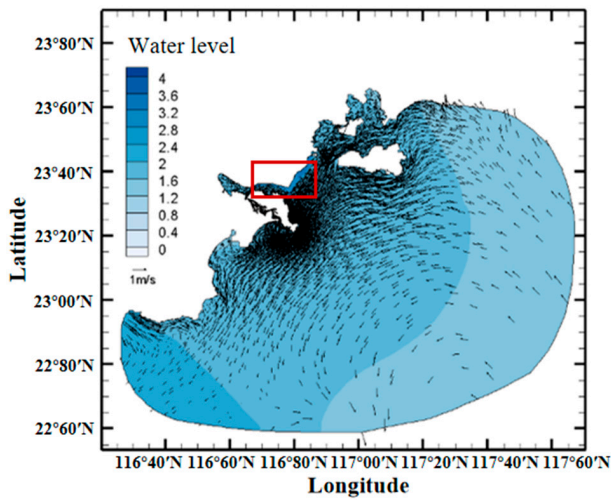

(**a**) Water level distribution with velocity vector in the whole study area at 2 h during storm surge
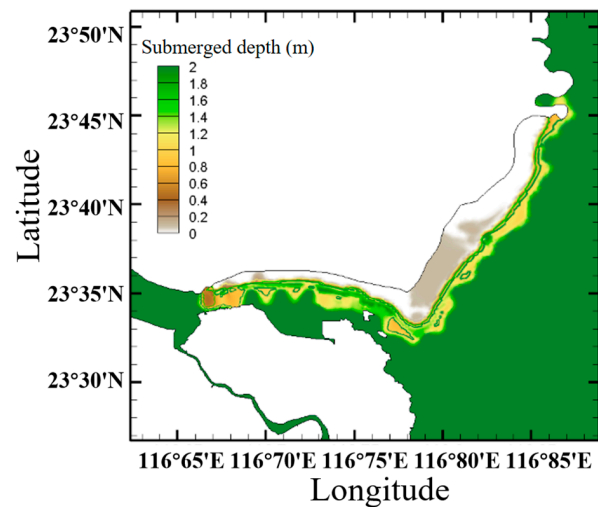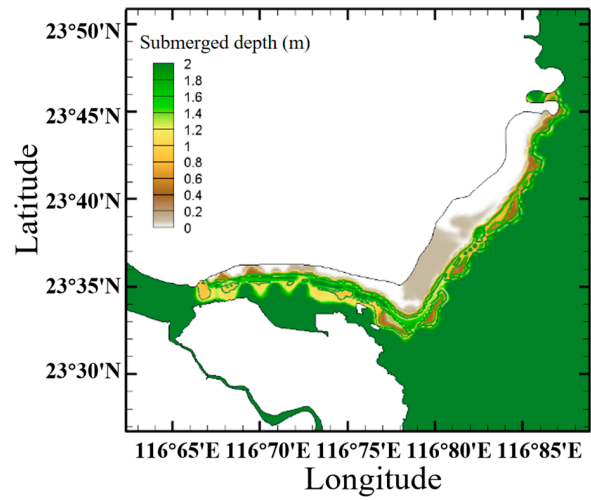

(**b**) The inundation range and depth of Rongjiang River Estuary and main urban area at 2 h during storm surge
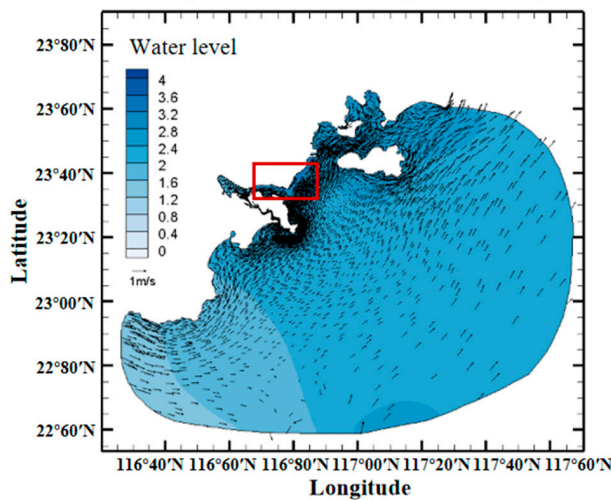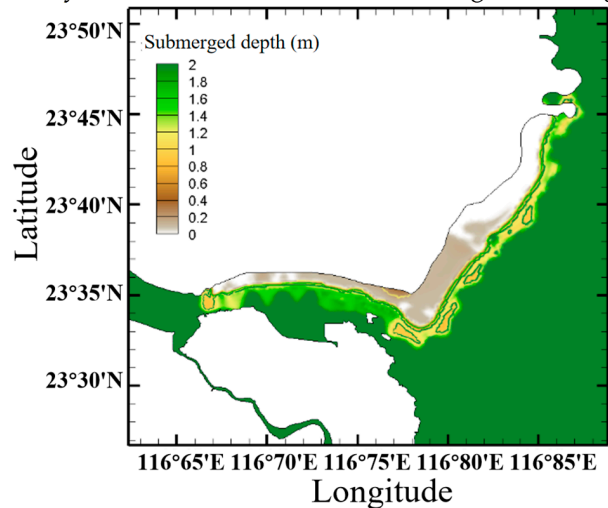
Figure 8. *Cont.*

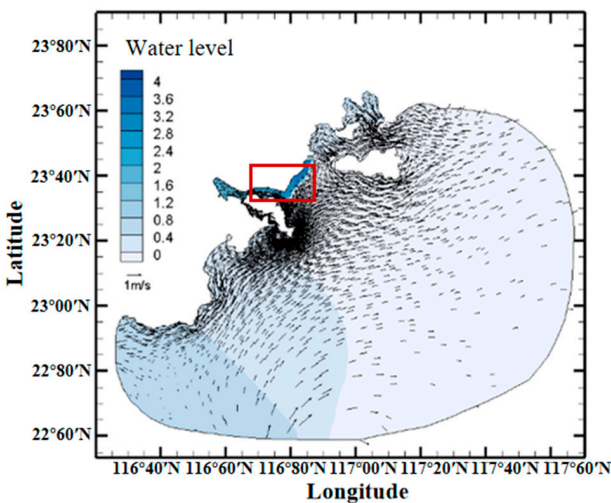(**c**) Water level distribution with velocity vector in the whole study area at 8 h during storm surge

(**d**) The inundation range and depth of Rongjiang River Estuary and main urban area at 8 h during storm surge

(**e**) Water level distribution with velocity vector in the whole study area at 14 h during storm surge

(**f**) The inundation range and depth of Rongjiang River Estuary and main urban area at 14 h during storm surge
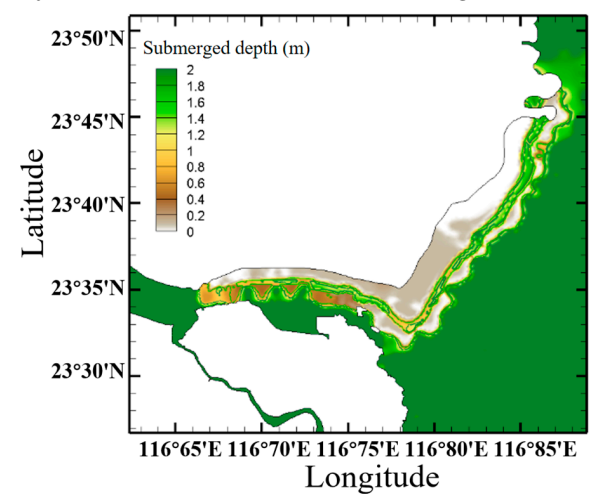
(**g**) Water level distribution with velocity vector in the whole study area at 20 h during storm surge

(**h**) The inundation range and depth of Rongjiang River Estuary and main urban area at 20 h during storm surge

Figure 8. Tidal current field and inundation of typhoon storm in 10-year return period (The red box on the left is the simulation area on the right).

In Figure 8, the left part is the water level distribution (based on the mean sea level of the Yellow Sea) and velocity vector diagram in the study area, and the right part is the inundation range and inundation depth near the Rongjiang Estuary and the main urban areas. The typhoon reached its maximum inundation 14 h ago, and the deepest accumulated water reached 0.38 m. During the 2 h of storm surge, the typhoon center did not match the study area. Still, under the wind, the water level in the study area obviously increased, especially in the northeast of Nan'ao Island, where the water level rose by more than 0.5 m. At 8 h, the typhoon center entered the study area. The water level gradient in the study area was high near the shore and low at the far shore, and the water level near the Rongjiang Estuary increased by nearly 1 m. At 14 h, the typhoon landed, and the hurricane was located northwest of the study area. The water level was high near the shore, low on the far shore, high in the northeast, and low in the southwest. The submerged area inside the dam expanded, but the accumulated water depth was still within 0.5 m. At 20 h, the typhoon center had left Shantou. However, the water level was still changing, and its distribution pattern was consistent with that in typical weather but nearly 0.2 m higher than in average temperature. In the Chenghai area, near the ocean dam, the outside water level dropped significantly, and the submerged area on the inside remained unchanged. Near the Rongjiang side, the water level outside the dam also dropped, and the inundation inside the dam no longer expanded. The inundation reached its maximum 14 h before, and the deepest accumulated water was 0.38 m. Since then, there was no further disaster expansion.

5.2. Analysis of the Protective Effect of Embankment on Storm Surge

It can be seen from the storm surge simulation in the 10-year-old situation that the bank can effectively keep out a large amount of seawater. When the typhoon intensity is vigorous, the seawater will cross the bank and enter the urban area. At the same time, after the typhoon transits, the seawater enters the landforms water in the bank instead because of the bank's existence. Figure 9 is a comparison chart of urban inundation degree with or without embankment under the condition of typhoon moving from southeast to northwest during the 10-year return period. The time is the maximum storm surge during the typhoon landing, and the height of the embankment is 1.5 m. It can be seen from the figure that the land in the study area is divided into two parts. One part is adjacent to the South China Sea, and the other is adjacent to the Rongjiang River in Shantou Bay, which can be regarded as the left and right parts of the V-shaped land. When there is no bank, the whole land in the study area will be submerged. The right part of the "V" shape will be submerged seriously, and the accumulated water depth can exceed 0.3 m, while the left part of the "V" shape is higher and far from the sea, and the submerged depth is about 0.1 m. When the bank is set, it can block part of the seawater intrusion, but it will form water near it. The bank can block part of the seawater when the storm surge is most substantial and play a protective role in inland areas.
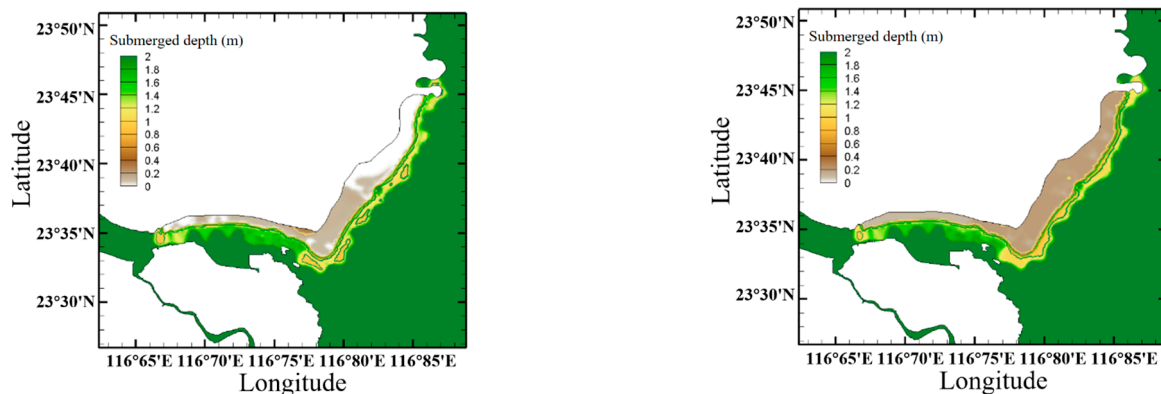
Figure 9. Blocking effect of bank on storm surge (the left picture shows the existence of bank, and the right picture shows the absence of bank).

Because the land topography is high, some seawater can flow back into the sea after the storm surge. At the same time, the water increase caused by the storm surge in the ocean will continue to fall back. However, due to the topographic conditions and embankment, part of the seawater will be left on the land. Figure 10 shows the water accumulation on the land when the typhoon is far away from the storm surge. The simulation results show that, in the case of no embankment, the left part of the V-shape is relatively high, and all the backward seawater flows back to the ocean. In contrast, the right part of the V-shape is relatively flat, and the amount of backward seawater is relatively large, so only some seawater can flow back. When there is a bank, the accumulated water on the land cannot enter the ocean due to the block of the bank but accumulates on the inner side of the bank, resulting in higher accumulated water, but less than 0.5 m.
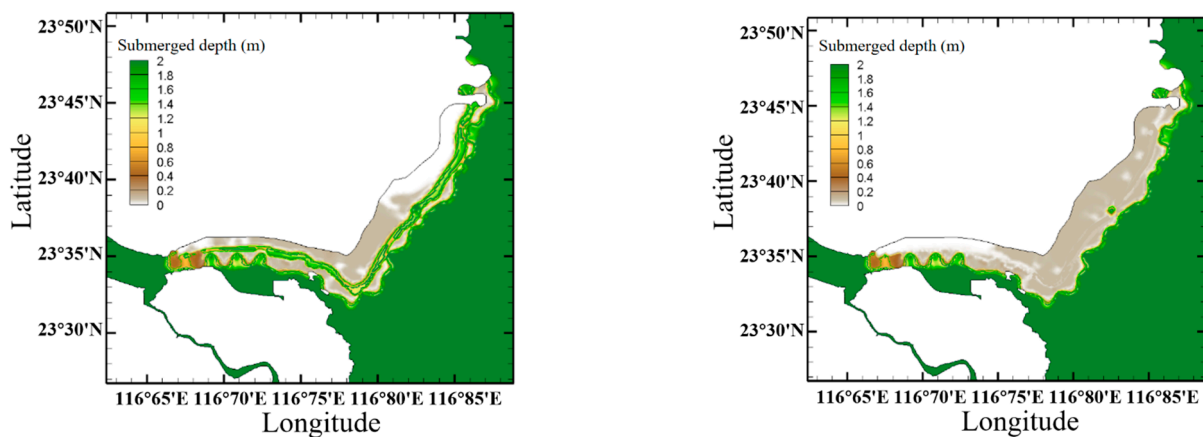
Figure 10. Water accumulation on land after typhoon transit (the left picture shows the existence of bank, and the right picture shows the absence of bank).

In summary, when a storm surge occurs, the bank can effectively block some seawater from entering the inland and play a better protective role. However, after the storm surge, the seawater entering the land will be blocked by the bank and gathered near the bank, which needs timely dredging.

In order to specifically analyze the blocking effect of the embankment on seawater during the storm surge, the right outside section of the V-shaped embankment was selected, and the changed seawater level and seawater velocity with the connecting distance were analyzed in both conditions. Take the landing time of the typhoon moving southeast-northwest in the 10-year return period as an example. The comparison of water levels in the sea area outside the embankment is shown in Figure 11. In the figure, a section with a length of 1000 m is selected at the shore bank on the seaside. The red line segment represents the offshore water level when there is a shore bank, and the blue line represents the offshore water level when there is no shore bank. Here, to visually compare the height of the water level, the location of the coastline is taken as the starting surface of the water level, namely 0 m. When there is a bank, the water level near the coastline can reach 1.4 m in this case. The seawater level stays relatively high with the increased offshore distance. However, when the distance is 400–500 m, the water level drops by nearly 0.4 m, which is consistent with the water level without a bank. Without a bank, the water level at the coastline reached 1.03 m under the action of storm surge, which means that the land was submerged by 1.03 m deep seawater at this time. Therefore, it can be said that the embankment significantly impacts the seawater level within 500 m, which is embodied in allowing for the high seawater to gather near the shore.
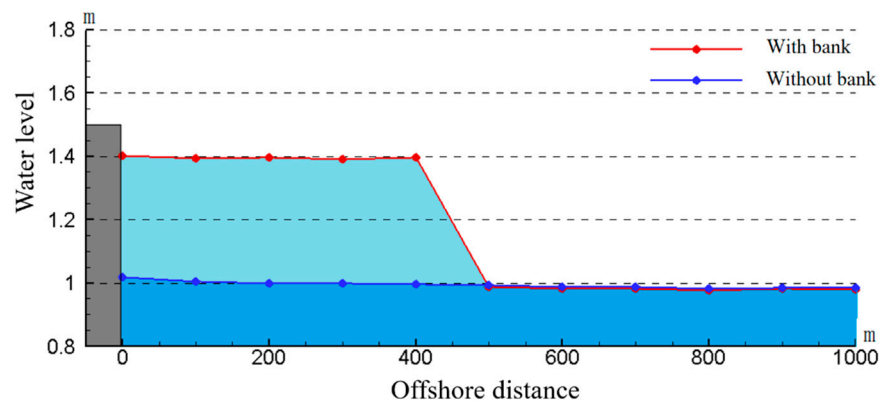
Figure 11. Comparison of water level in the sea area outside the embankment.

The result of comparing the velocity of Shanghai water in the same profile is shown in Figure 12. When there is a bank, because of the barrier of the bank near the coastline, the seawater has no velocity component perpendicular to the shoreline, and the velocity there is small, only 0.21 m/s. With the increased distance from the shore, the velocity of seawater increases in an oscillating way, and the velocity can reach the maximum value of 0.49 m/s at 300 m ashore. After that, the flow rate decreases, reaching the lowest value at 500 m. After 600 m, it becomes stable, and the flow rate is between 0.3 m/s and 0.4 m/s. Under the condition of no bank, the flow rate of seawater in the sea area changes little, and the flow rate on the coastline is faster than that under the condition of no bank. At 600 m, there is a bank gradually approaching the flow rate under the condition of no bank, and at 800 m, the two flow rates are the same, and the changing trend is the same after that.
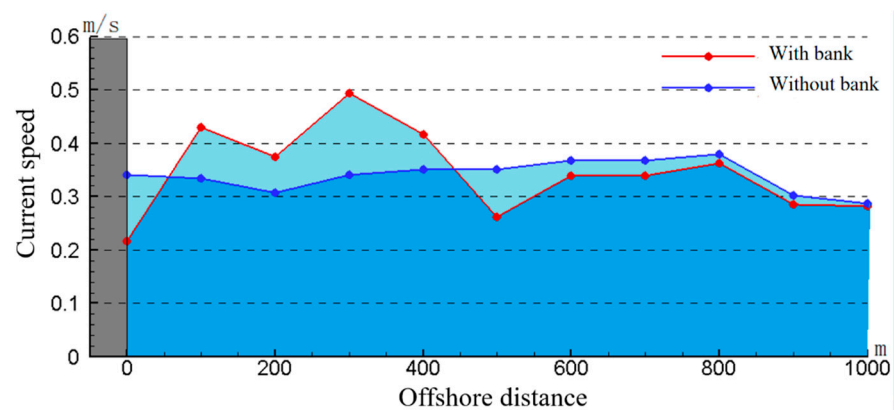

Figure 12. Comparison of velocity in sea area outside embankment.

According to the simulation results, given the typhoon with the intensity of a ten-year return period, the shore dike can effectively block a large amount of seawater when the storm surge occurs. However, due to the function of the shore dike, the offshore water level within 500 m will rise by an additional 0.4 m. When the storm surge is over, the shore dike will cause the seawater entering the land to accumulate water at the shore dike, which needs to be dredged in time. Embankment also has an impact on the velocity of the external sea area within 600 m during a storm surge, resulting in an overall increase of 0.16 m/s in seawater velocity. Generally speaking, the embankment will only work on a specific range of offshore areas.

6. Sediment Deposition in Shantou

6.1. Simulation Results of Main Siltation Areas

Figure 13 shows the sediment deposition in the study area over five years. It can be seen that there are four main siltation areas, which are located at Waishahe Estuary,

Hanjiang Xixi Estuary, Rongjiang Estuary, and Shantou Port waterway. From the shape of the sedimentary area, the sediments in the three estuaries are all fan-shaped because of the exact sediment deposition mechanism. The Hanxixi Estuary is in a regular fan shape; the Waishahe Estuary and Rongjiang Estuary show an irregular sector, with thicker deposits in the southwest of Waishahe Estuary and vaster deposits in the northeast of Rongjiang Estuary. There are several siltation areas in Shantou Bay, but the siltation degree is lighter than that at the estuary. The siltation in the bay can be divided into two parts: The first is the siltation area near the inland river. The main feature of deposition here is that the deposition range is extensive, but the deposition thickness is small. The second part of the siltation is concentrated on the side near the ocean, showing the trend of cutting off the river. This part of siltation is concentrated and small in area but thick in thickness.
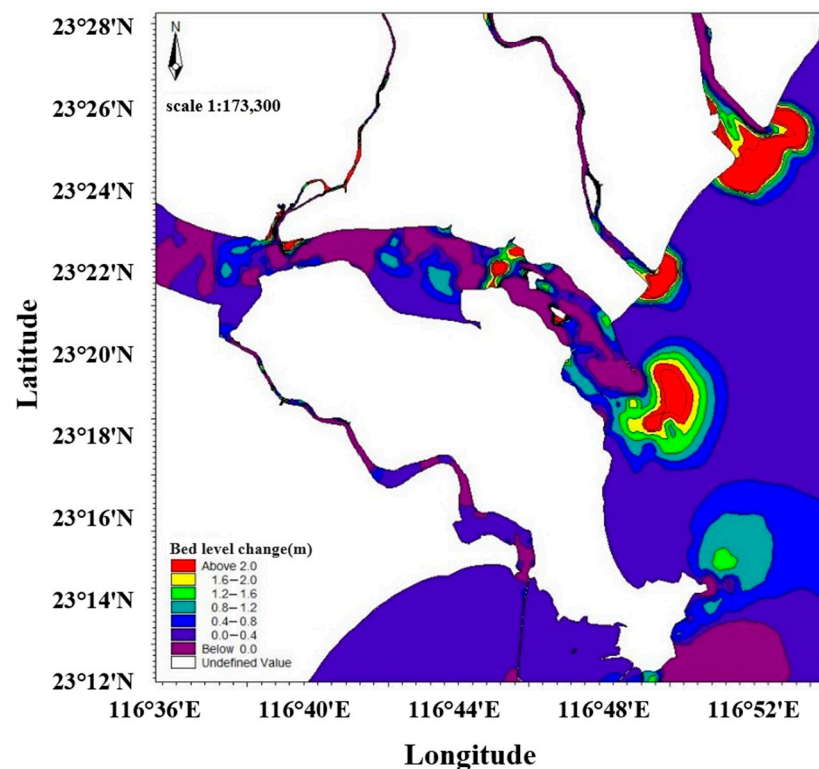

Figure 13. Overall siltation in the study area.

Figures 14–17 shows the enlarged views and 5-year changes of siltation thickness of Waishahe Estuary, Hanjiang Xixi Estuary, Rongjiang Estuary, and Shantou Port Channel, respectively, to facilitate the analysis of siltation in the study area. Hanxi River and Waisha River are both branches of the Hanjiang River, so the law of sediment deposition is the same, and the variation curve of sediment thickness in five years is similar.

However, the runoff of Hanjiang Xixi is smaller than that of Waisha River, so the sediment is easier to deposit, and the final deposition thickness is higher than that of the Waisha River Estuary. The central axis of the area where the sediment of Hanxixi Estuary exceeds 1 m is about 1560 m, and the sediment area is about 0.96 km^2.

Tides control Rongjiang Estuary and Shantou Bay, and the short-term siltation rates of Rongjiang Estuary and Shantou Bay show periodic changes. A period of 15 days is consistent with the astronomical tide period, indicating that it is highly correlated with the astronomical tide, which is in line with reality. Because of the breakwater in the Rongjiang Estuary, the sediment deposition is different under the ebb and flow tide, forming two settlement centers. The reference point selected by Rongjiang Estuary is located at the sedimentation center outside the sand dike. Different from the Waisha River and Hanjiang Xixi River, the sedimentation rate at the sand dike of Rongjiang Estuary is very uniform

and generally increases linearly. Two representative locations in Shantou Port are selected for analysis. The red line segment is the silting area near the sea, and the blue line is the main silting center on the inland river. The sedimentation trend of the two places is the same, but the sedimentation rate near the seaside is faster. The siltation rate in Shantou Bay is decreasing yearly because the siltation in Shantou Bay is more controlled by tides, while the siltation at Rongjiang Estuary and the siltation at the channel reduce the tide carrying sediment into the bay. Therefore, unlike Rongjiang Estuary, the siltation rate in Shantou Bay, which is also controlled by tides, is decreasing yearly.
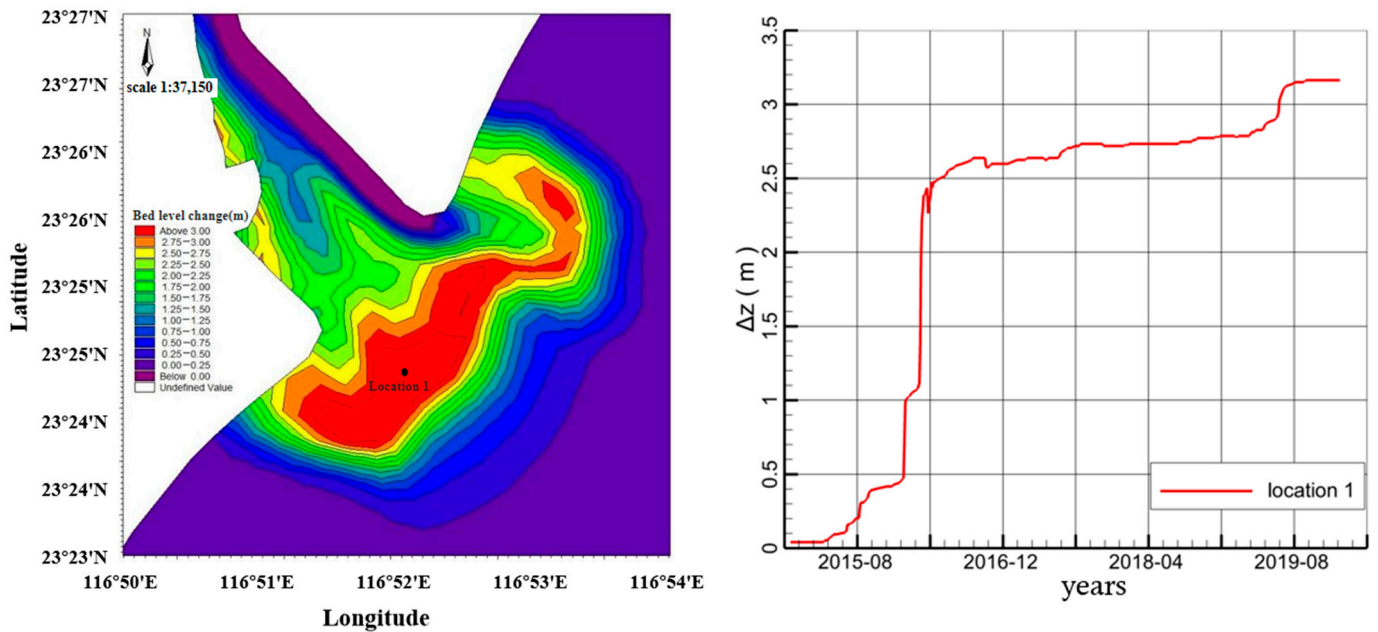

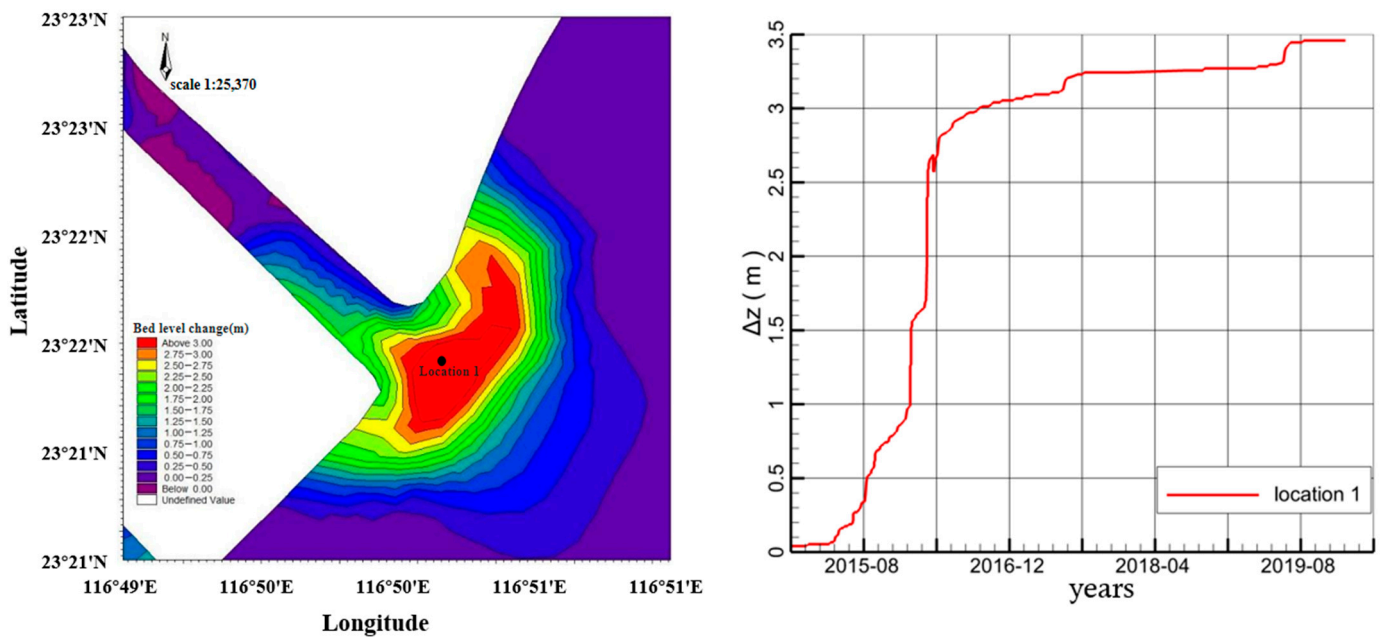**Figure 14.** Changes of sedimentation thickness of Waishahe in 5 years.

Figure 15. Changes of sedimentation thickness in Hanjiang Xixi Estuary in 5 years.
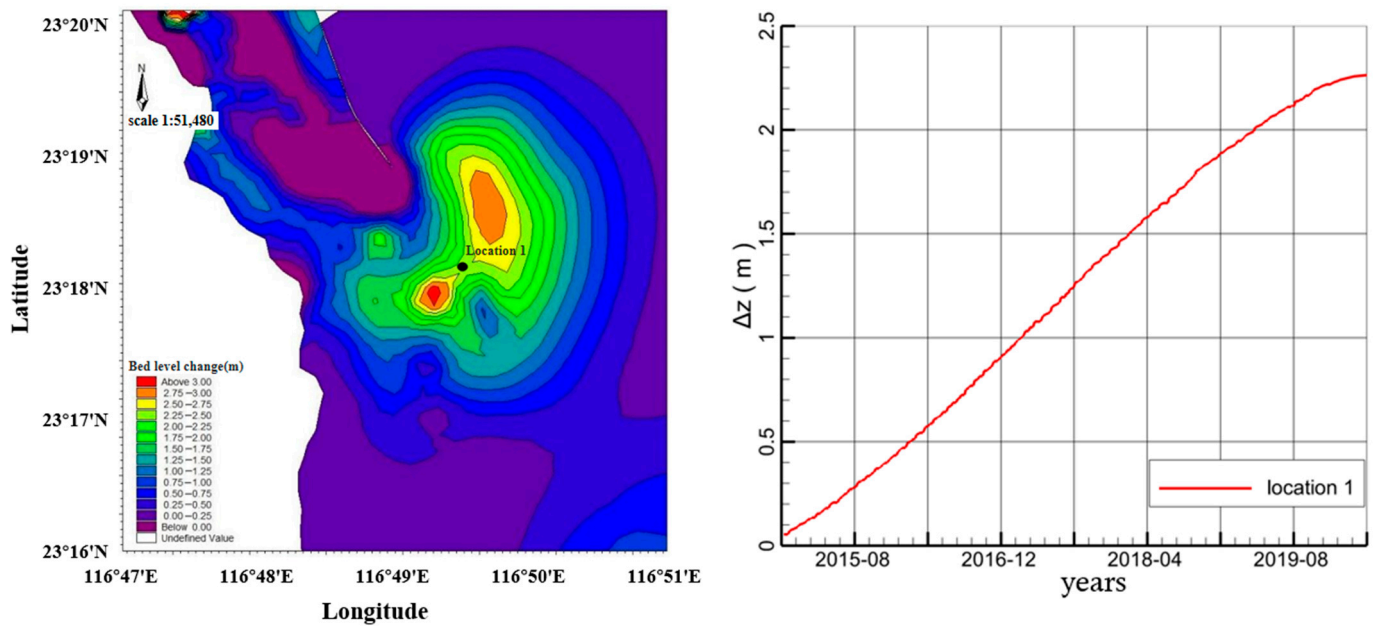
Figure 16. Changes of sedimentation thickness in Rongjiang Estuary in 5 years.
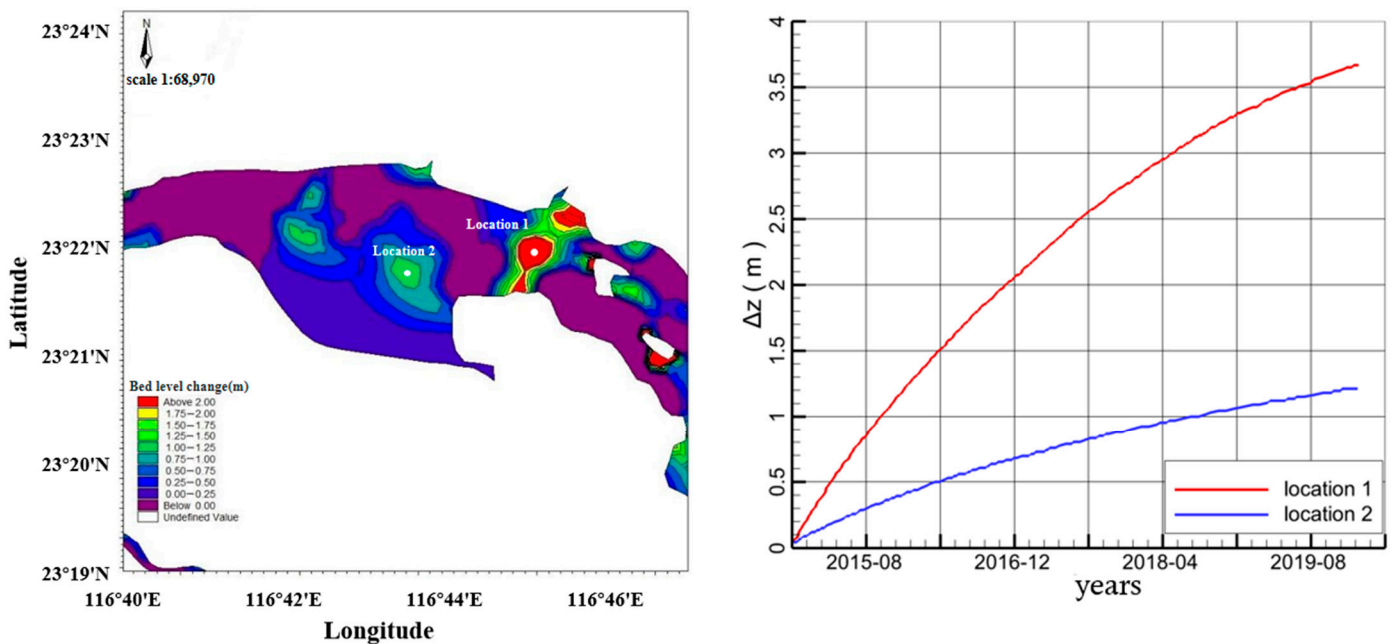

Figure 17. Changes of sedimentation thickness in Shantou Bay in 5 years.

6.2. Discuss the Causes of Siltation in Shantou Bay

Although the siltation range of Shantou Bay is not extensive, the siltation by sea survey will block the river, affect the regular shipping operation, and is not conducive to Shantou's foreign economy and trade. Therefore, it is of far-reaching significance to analyze the causes of siltation in Shantou Bay for the future development of Shantou. Figure 17 shows that the siltation in Shantou Bay is controlled by the tide, which is the decisive factor, but the source of siltation needs further discussion. When rivers flood, the water flow is large, and the sediment content is significant, so the siltation in the study area changes significantly at this time. Therefore, this paper analyzes the influence of rivers on sediment deposition in Shantou Bay from the changes of sediment bodies in Shantou Bay under the historical flood discharge time of each river.

In terms of sediment sources, the sediment sources of Shantou Port mainly include three parts:

- Sediment directly from the Rongjiang River;
- Sediment from the Hanjiang River through Meixi;
- Sediment from the ocean under the action of the tide.

Therefore, the historical flood discharge time of the Rongjiang River and Hanjiang Rivers is selected to analyze the siltation areas of Shantou Bay one by one.

For the Rongjiang River, a typical sluice opening and discharging process of the Rongjiang River from 15 August 2016 to 20 August 2016 was selected for analysis. Figure 18 shows the thickness of the siltation body before and after the flood peak here. It can be seen from Figure 18 that after the large-scale flood discharge in the upper reaches of the Rongjiang River, and the maximum siltation area near the inland riverside has increased to some extent. In contrast, the siltation near the seaside has no noticeable change. This shows that the sediment brought by the flood discharge of the Rongjiang River settled before it entered the estuary. It can be judged that Rongjiang's contribution to Shantou Port's siltation will be more negligible if it is not during flood discharge. The siltation contribution of Rongjiang River to Shantou Port mainly occurred during the sluice opening in the upper reaches of Rongjiang River, which mainly acted on the silts near the inland river but made little contribution to the silts near the sea.
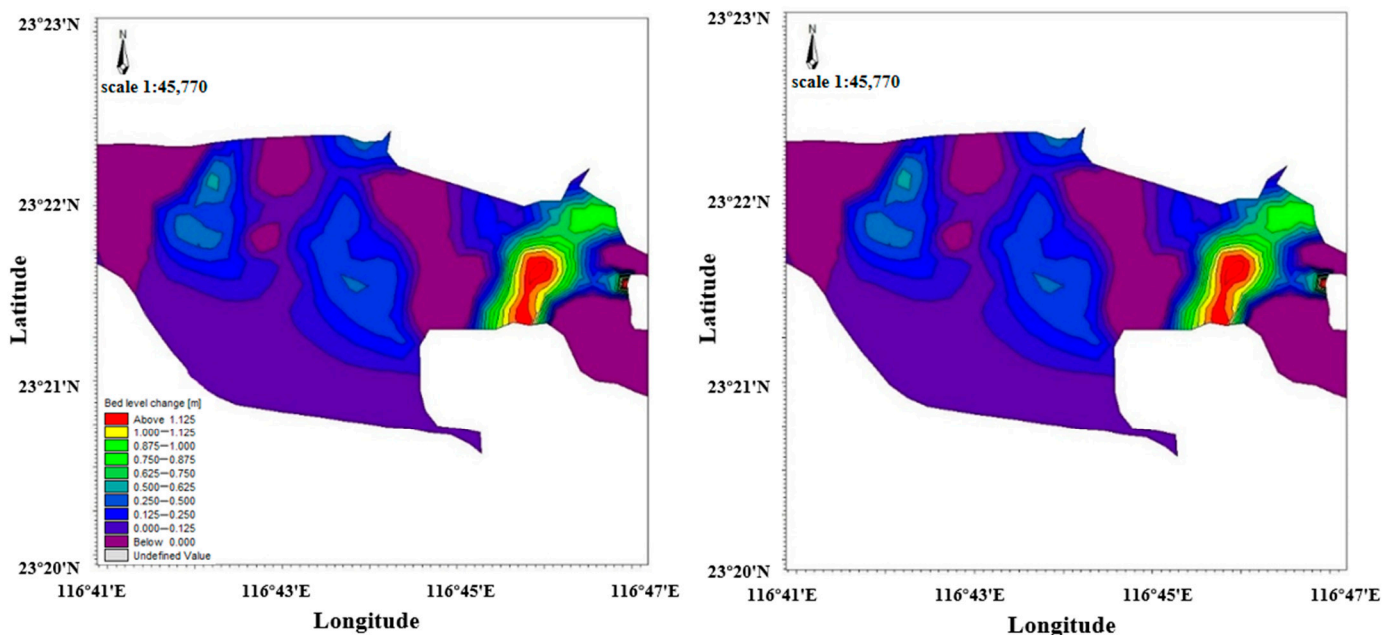

Figure 18. Changes of silts in Shantou Port before and after flood discharge of Rongjiang River.

The flood discharge of the Hanjiang River and Rongjiang River should be around the 20th of that month to avoid the difference in tidal conditions. Figure 19 shows the comparison of sediment deposition in Shantou Port before and after the flood discharge of Hanjiang River, which is 0:00 on 18 October 2016 and 23:00 on 23 October 2016, respectively. During this period, there is no other flood discharge, and it can be seen that the maximum sedimentation area of the whole sediment body has expanded. Meixi connects Han River and Shantou Port, so Meixi, which directly affects sediment deposition in Shantou Port, is selected for analysis. According to the inspection, the flood discharge of Hanjiang River can reach 670 m^3/s, and that of Meixi River is only about 5%, that is, less than 40 m^3/s, which is less than 20% of that of Rongjiang River. The discharge of the Meixi River is much smaller than that of the Rongjiang River, but the degree of siltation after flood discharge is greater. Therefore, it can be judged that the Hanjiang River has contributed to the siltation of Shantou Port.
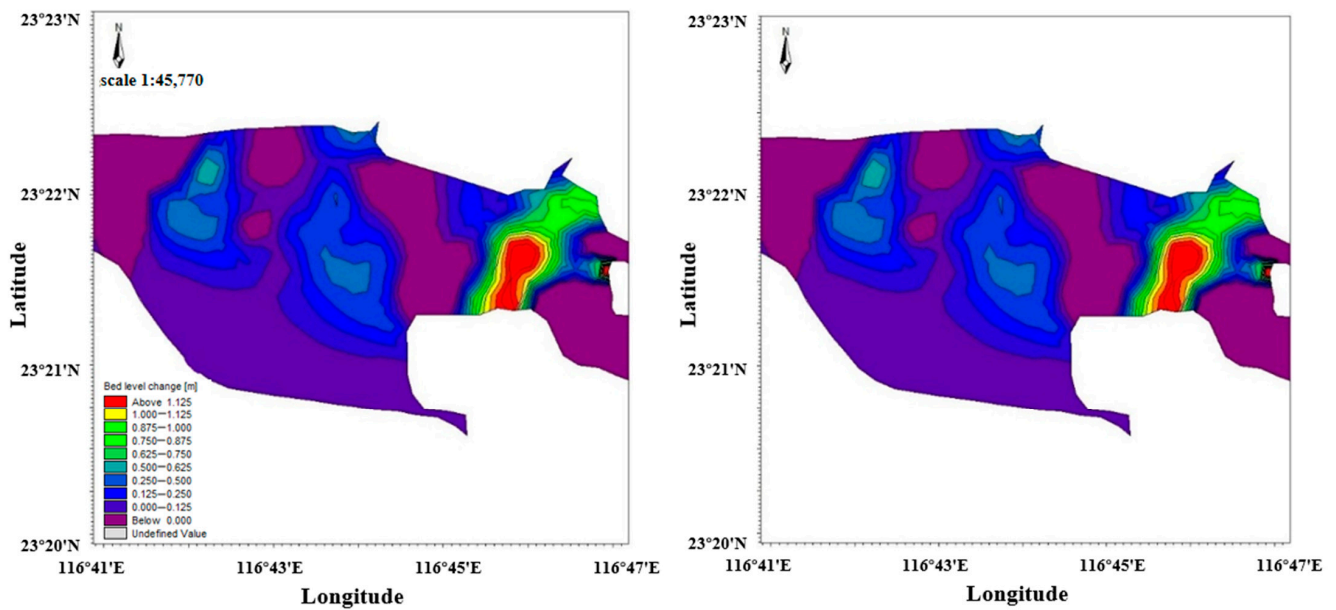
Figure 19. Changes of silts in Shantou Port before and after flood discharge of Hanjiang River.

To further discuss the contribution and deposition mechanism of Hanjiang River to Shantou Port, the siltation of Shantou Port before and after the removal of Hanjiang River sediment in one year, and the siltation at Meixi before and after the flood discharge of Hanjiang River in October 2016 were simulated.

Figure 20 to remove the siltation of Shantou Port before and after one year's sediment load of Hanjiang River, the left figure shows the actual siltation situation. The correct figure shows that the sediment load of Hanjiang River is set to 0, and other conditions are consistent to compare the siltation situation of Shantou Port in one year. The sediment deposition in Shantou Port on the right will be reduced to a certain extent, and the sedimentation in the whole area is relatively slow. However, the overall trend has mostly stayed the same. Therefore, it can be concluded that the Hanjiang River contributes to the siltation of Shantou Port, but it is not the decisive factor.
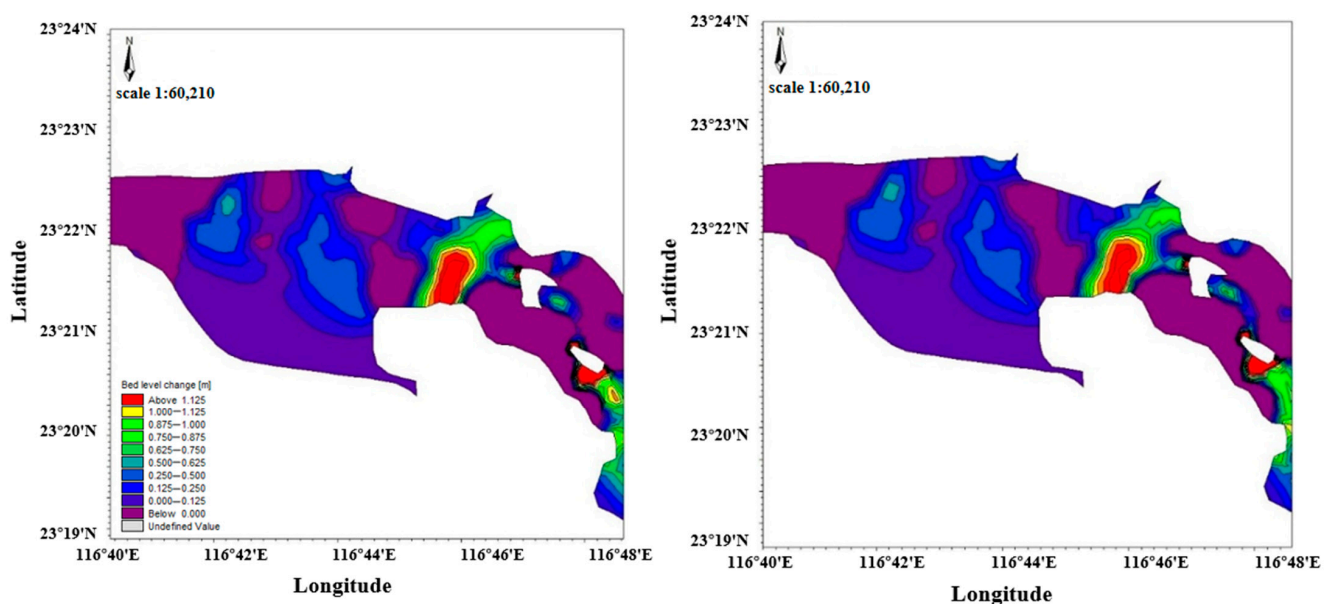

Figure 20. Comparison of Hanjiang River's contribution to Shantou Port's siltation. The left picture shows the real state, and the right picture shows that Hanjiang River's silt is set to 0.

Figure 21 shows the change in sediment deposition in the Meixi Estuary before and after the flood discharge. Before the flood discharge in the left picture, it can be seen that there are two prominent silting areas in the Meixi River when it enters the Rongjiang River. In comparison, the silting thickness in the two areas in the right picture has increased after the flood discharge. According to the hydrodynamic conditions of the Hanjiang River and Rongjiang River, the discharge and velocity of the Hanjiang River are much higher. Combined with Figure 21, it can be concluded that the sediment from the Hanjiang River settles after entering the Rongjiang River through the Meixi River, resulting in a deposition at Meixi Estuary. At the same time, the rest continues to be transported downstream. Most of the sediment brought by the single flood discharge of the Hanjiang River settled at the mouth of the Meixi River, and a small part settled in the Rongjiang River.
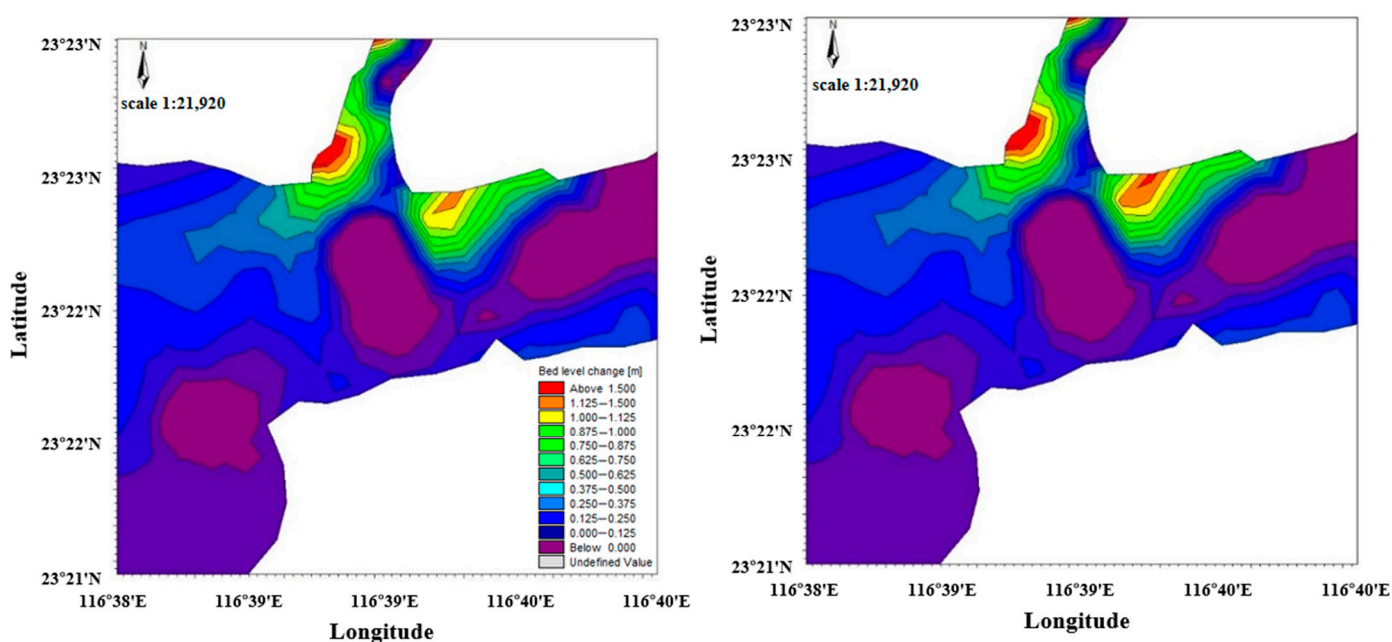

Figure 21. Sediment deposition at Meixi before and after flood discharge.

To sum up, the causes and laws of siltation in Shantou Port are summarized. Sediment sources in Shantou Port include the Rongjiang River, Hanjiang River, and tidal current. Under normal conditions, the Rongjiang River has a small flow rate, slow flow rate, and low sediment load, which does not affect the siltation of Shantou Port. During flood discharge, the sediment of the Rongjiang River mainly settles on the inland river side of Shantou Port. The Hanjiang River has a significant flow rate, a fast flow rate, and a high sediment content, and flows into the Rongjiang River through the Meixi River. However, most of the sediment of the Hanjiang River settles and accumulates at the mouth of the Meixi River after entering the Rongjiang River. Only part of it enters Shantou Port with the Rongjiang River, which contributes to the sedimentation of both parts of Shantou Port, but there are other factors besides this. The decisive factor of sediment deposition in Shantou Port is the sediment entering the port through ocean tides.

7. Conclusions

The main conclusions of this paper are as follows:

(1) For a typhoon with a 10-year return period, the embankment can effectively block a large amount of seawater in the ocean and prevent seawater from entering the land. At the same time, when the storm surge is over, the seawater entering the ground will not flow back to the ocean smoothly, and water will accumulate at the bank, quickly leading to the aggravation of the post-disaster cleaning task.

(2)　Due to the effect of the embankment, the offshore water level will rise by an additional 0.4 m, resulting in an overall increase of the seawater velocity by 0.16 m/s.

(3)　The main siltation areas of Shantou are located in various estuaries and Shantou Port Channel. The siltation of the Xixi Estuary and Waisha Estuary of Hanjiang River is controlled by runoff, while tides prevent the siltation of Shantou Port Channel and Rongjiang Estuary.

(4)　The decisive factor of sediment deposition in Shantou Port is the sediment entering the port through ocean tides. During the flood discharge of the Rongjiang River, most of the residue is deposited on the inland river side of Shantou Port. During the flood discharge of the Hanjiang River, Meixi played a role in the siltation of Shantou Port, contributing to the siltation of two parts of Shantou Port, and Hanjiang River contributed more to the siltation of Shantou Port than Rongjiang River.

Author Contributions: Data curation, E.Z. and W.W.; formal analysis, Y.W. (Yuxi Wu) and E.Z.; funding acquisition, Y.W. (Yang Wang) and R.J.; investigation, J.Y., K.Z., H.W. and H.Q.; project administration, Y.W. (Yang Wang) and Z.S.; writing—original draft, Y.W. (Yuxi Wu); writing—review and editing, K.Z. All authors have read and agreed to the published version of the manuscript.

Institutional Review Board Statement: Not applicable.

Informed Consent Statement: Not applicable.

Data Availability Statement: Wind field data are from the European Centre for Medium-Range Weather Forecasts. Here is the link: https://cds.climate.copernicus.eu (accessed on 11 July 2021).

Conflicts of Interest: The authors declare no conflict of interest. The funders had no role in the design of the study; in the collection, analyses, or interpretation of data; in the writing of the manuscript, or in the decision to publish the results.

References

1.　Hou, Y.; Yin, B.; Guan, C.; Guo, M.; Liu, G.; Hu, P. Research progress and prospect of marine dynamic disasters in China. *Oceanol. Limnol. Sin.* **2020**, *51*, 759–767.

2.　Hu, X.; Yu, H.; Yu, M. Causes and comparative analysis of offshore strengthening of Typhoon Hagupit. *Mod. Agric. Sci. Technol.* **2021**, *9*, 187–190.

3.　Shan, C. Response and enlightenment of typhoon "Tian Ge". *Labor Prot.* **2019**, *9*, 39–41.

4.　Luo, W.; Song, L.; He, R.; Li, J. Investigation report on urban complex disasters caused by typhoon Mangosteen. *Zhejiang Water Conserv. Sci. Technol.* **2019**, *47*, 16–18.

5.　Feng, S. *Introduction to Storm Surge*; Science Press: Beijing, China, 1982.

6.　Cai, W. Characteristics of storm surge along Shantou coast. *Sci. Technol. Commun.* **2013**, *5*, 113+111.

7.　Bian, J. Numerical Simulation of Coastal Typhoon Storm Surge and Extreme Value Analysis of Water Increase. Master's Thesis, Yangzhou University, Yangzhou, China, 2019.

8.　Shen, Y. Numerical Simulation of Storm Surge in Bohai Sea. Master's Thesis, Dalian University of Technology, Dalian, China, 2018.

9.　Wang, Y.; Mao, X.; Jiang, W. Long-term hazard analysis of destructive storm surges using the ADCIRC-SWAN model: A case study of Bohai Sea, China. *Int. J. Appl. Earth Obs. Geoinf.* **2018**, *73*, 52–62. [CrossRef]

10.　Suh, S.W.; Lee, H.Y.; Kim, H.J.; Fleming, J.G. An efficient early warning system for typhoon storm surge based on time-varying advisories by coupled ADCIRC and SWAN. *Ocean. Dyn.* **2015**, *65*, 617–646. [CrossRef]

11.　Zaman, S.; Mondal, M.S. Risk-based determination of polder height against storm surge hazard in the south-west coastal area of Bangladesh. *Prog. Disaster Sci.* **2020**, *8*, 100131. [CrossRef]

12.　Jelesnianshi, C.P.; Chen, J.; Wilson, A. *SLOSH: Sea, Lake and Overland Surges from Hurricanes*; NOAA Technical Report; NWS: Miami, FL, USA, 1992; Volume 48, p. 711992.

13.　Watson, C.; Johnson, E. Design, implementation and operation of a modular integrated tropical cyclone hazard model: Caribbean disaster mitigation project. In Proceedings of the 23rd Conference on Hurricanes and Tropical Meteorology, Dallas, TX, USA, 10–15 January 1999.

14. Shu, G. Green seawall blueprint for preventing future storm surge disasters. *Science* **2020**, *106*, 14–16.

15. Dai, L.; Zhang, Y. Yancheng Erosion Coastal Protection Design. *Prog. Water Conserv. Hydropower Sci. Technol.* **2009**, *3*, 50–53.

16. Wang, C. *Research on the Construction of Coastal Protection Embankment in Weifang Binhai Development Zone*; Shandong University: Jinan, China, 2013.

17. Shi, S.; Yang, B.; Jiang, W. Numerical simulations of compound flooding caused by storm surge and heavy rain with the presence of urban drainage system, coastal dam and tide gates: A case study of Xiangshan, China. *Coast. Eng.* **2022**, *172*, 104064. [CrossRef]

18. Ma, G.; Han, Y.; Niroomandi, A.; Lou, S.; Liu, S. Numerical study of sediment transport on a tidal flat with a patch of vegetation. *Ocean. Dyn.* **2015**, *65*, 203–222. [CrossRef]

19. Arslan, M.; JingCheng, H.; Wajid, I.M.; Ali, S.A.; Muhammad, A.; Maryam, Y. Impact of Sediment Deposition on Flood Carrying Capacity of an Alluvial Channel: A Case Study of the Lower Indus Basin. *Water* **2022**, *14*, 3321.

20. Zhao, E.J.; Dong, Y.K.; Tang, Y.Z.; Cui, L. Numerical study on hydrodynamic load and vibration of pipeline exerted by submarine debris flow. *Ocean. Eng.* **2021**, *239*, 109754. [CrossRef]

21. Zhao, E.J.; Shi, B.; Qu, K.; Dong, W.B.; Zhang, J. Experimental and Numerical Investigation of Local Scour around Submarine Piggyback Pipeline under Steady Currents. *J. Ocean. Univ. China* **2018**, *17*, 244–256. [CrossRef]

22. Zhao, E.J.; Qu, K.; Mu, L. Numerical study of morphological response of the sandy bed after tsunami-like wave overtopping an impermeable seawall. *Ocean. Eng.* **2019**, *186*, 106076. [CrossRef]

23. Zhao, E.J.; Dong, Y.K.; Tang, Y.Z.; Sun, J.K. Numerical investigation of hydrodynamic characteristics and local scour mechanism around submarine pipelines under joint effect of solitary waves and currents. *Ocean. Eng.* **2021**, *222*, 108553. [CrossRef]

24. Qi, Y. *Numerical Simulation Analysis of Sediment Deposition in Yazidung Reservoir and Study on Sediment Regulation Scheme*; Xi'an University of Technology: Xi'an, China, 2019.

25. Christelle, A.; Jean-Roch, N.; Philip, M.; Irene, P.; Remo, C. Modelling the influence of Tidal Energy Converters on sediment dynamics in Banks Strait, Tasmania. *Renew. Energy* **2022**, *88*, 1105–1119.

26. Yuan, S.; Yuan, P.; Si, X.; Tan, J.; Wang, S.; Liu, X. Numerical simulation of tidal current in Bohai Sea and Yellow Sea based on FVCOM. *Bull. Ocean. Lakes* **2020**, *2*, 10–18.

27. Chu, L.; Ceng, Z. Sedimentation characteristics and development trend of Shantou Port. *Trop. Geogr.* **1983**, *3*, 1–7.

28. Huang, L. Summary of Sediment Source and Phase I Regulation Project of Shantou Port Outer Channel. *Waterw. Eng.* **2001**, *7*, 55–57.

29. Chen, C.; Beardsley, R.; Cowles, G. An unstructured grid, finite-volume coastal ocean model (FVCOM) system. *Oceanography* **2006**, *9*, 78–89. [CrossRef]

30. Li, R. *Numerical Solution of Partial Differential Equations*; Higher Education Press: Beijing, China, 2005.

31. Graham, H.E.; Nunn, D.E. *National Hurricane Research Project, Report No.33: Meteorological Conditions Pertinent to Standard Project Hurricane Atlantic and Gulf Coasts of the United States*; US Department of Commerce and Weather Bureau: Washington, DC, USA, 1959.

32. Tang, J.; Shi, J.; Li, X.; Deng, B.; Jin, M. Numerical simulation of typhoon waves based on typhoon wind field model. *Ocean. Lake Bull.* **2013**, *2*, 24–30.

33. Jiang, Z.; Hua, F.; Qu, P. A new tropical cyclone parameter adjustment scheme. *Adv. Mar. Sci.* **2008**, *1*, 1–7.

34. Willoughby, H.E.; Rahn, M.E. Parametric representation of the primary hurricane vortex. Part I: Observations and evaluation of the Holland (1980) model. *Mon. Weather Rev.* **2004**, *132*, 3033–3048. [CrossRef]

35. Atkinson, G.D.; Holliday, C.R. Tropical cyclone minimum sea level pressure/maximum sustained wind relationship for the western North Pacific. *Mon. Weather Rev.* **1977**, *105*, 421–427. [CrossRef]

36. Tang, Y.; Wang, Y.; Zhao, E.; Yi, J.; Feng, K.; Wang, H.; Wang, W. Study on Hydrodynamic Characteristics and Environmental Response in Shantou Offshore Area. *J. Mar. Sci. Eng.* **2021**, *9*, 912. [CrossRef]

37. Gao, J.; Ma, X.; Dong, G.; Chen, H.; Liu, Q.; Zang, J. Investigation on the effects of Bragg reflection on harbor oscillations. *Coast. Eng.* **2021**, *170*, 103977. [CrossRef]

38. Gao, J.; Ma, X.; Zang, J.; Dong, G.; Ma, X.; Zhu, Y.; Zhou, L. Numerical investigation of harbor oscillations induced by focused transient wave groups. *Coast. Eng.* **2020**, *158*, 103670. [CrossRef]